

Article

Sea Clutter Suppression Method Based on Ocean Dynamics Using the WRF Model

Guigeng Li ¹, Zhaoqiang Wei ^{2,*}, Yujie Chen ¹, Xiaoxia Meng ¹ and Hao Zhang ^{1,3}

¹ Faculty of Information Science and Engineering, School of Electronic Engineering, Ocean University of China, Qingdao 266100, China; liguigeng@stu.ouc.edu.cn (G.L.); chenyj@qdhc.edu.cn (Y.C.); zhanghao@ouc.edu.cn (H.Z.)

² Institute for Advanced Ocean Study, Ocean University of China, Qingdao 266100, China

³ Department of Electrical and Computer Engineering, University of Victoria, Victoria, BC V8W 2Y2, Canada

* Correspondence: weizhaoqiang@ouc.edu.cn

Abstract: Sea clutter introduces a significant amount of non-target reflections in the echo signals received by radar, complicating target detection and identification. To address the challenge of existing filter parameters being unable to adapt in real-time to the characteristics of sea clutter, this paper integrates ocean numerical models into the sea clutter spectrum estimation. By adjusting filter parameters based on the spectral characteristics of sea clutter, the accurate suppression of sea clutter is achieved. In this paper, the Weather Research and Forecasting (WRF) model is employed to simulate the ocean dynamic parameters within the radar detection area. Hydrological data are utilized to calibrate the parameterization scheme of the WRF model. Based on the simulated ocean dynamic parameters, empirical formulas are used to calculate the sea clutter spectrum. The filter coefficients are updated in real-time using the sea clutter spectral parameters, enabling precise suppression of sea clutter. The suppression algorithm is validated using X-band radar-measured sea clutter data, demonstrating an improvement factor of 17.22 after sea clutter suppression.

Keywords: ocean dynamics; shore-based radar; WRF model; sea clutter suppression; sea clutter spectrum; digital filter



Academic Editors: Christos Tsabaris and Gabriele Pieri

Received: 24 December 2024

Revised: 19 January 2025

Accepted: 21 January 2025

Published: 25 January 2025

Citation: Li, G.; Wei, Z.; Chen, Y.; Meng, X.; Zhang, H. Sea Clutter Suppression Method Based on Ocean Dynamics Using the WRF Model. *J. Mar. Sci. Eng.* **2025**, *13*, 224. <https://doi.org/10.3390/jmse13020224>

Copyright: © 2025 by the authors. Licensee MDPI, Basel, Switzerland. This article is an open access article distributed under the terms and conditions of the Creative Commons Attribution (CC BY) license (<https://creativecommons.org/licenses/by/4.0/>).

1. Introduction

For marine target detection radars, the backscatter from the sea surface, when illuminated by radar, often significantly affects the radar's ability to detect and identify targets such as ships, aircraft, missiles, navigational buoys, and other objects located within the same radar resolution cell as the sea surface. These interfering signals are referred to as sea clutter. Compared to land clutter, sea clutter is more complex due to the dynamic nature of the sea surface, which is influenced by natural factors such as wind speed, waves, humidity, temperature, and tides.

The intensity and spectral characteristics of sea clutter are significantly influenced by the radar operating frequency, the polarization mode, and the angle of electromagnetic wave incidence. An increase in radar operating frequency enhances sensitivity to small-scale ocean surface waves, resulting in higher amplitude sea clutter received by high-frequency radars compared to their low-frequency counterparts. The polarization mode affects the strength and distribution of sea clutter echoes; horizontal polarization more effectively captures wave reflections from the sea surface, while vertical polarization is more sensitive to wave crests [1]. The angle of incidence of radar waves is a critical factor influencing sea clutter characteristics, with lower grazing angles typically generating

stronger sea clutter due to the complex multiple scattering and reflection experienced as radar waves approach the sea surface. As the grazing angle increases, the intensity of sea clutter gradually diminishes. A thorough investigation of these influencing factors can enhance the understanding of sea clutter's interference with maritime target detection and recognition, thereby improving the detection accuracy of radar systems.

Sea clutter modeling involves establishing relationships between sea clutter characteristics and radar parameters, as well as ocean environmental parameters, to understand the temporal and spatial variations of sea clutter [2,3]. Sea clutter can be modeled from multiple dimensions. Traditional modeling methods rely on measured sea clutter data and employ statistical techniques to develop relevant parameterized models [4]. Typical sea clutter models include the backscattering coefficient model for the sea surface [5,6], amplitude statistical models [7,8], polarization models [9,10], and Doppler spectrum models [11].

As the sea surface presents an incessant state of motion, combined with the influences of antenna scanning modulation and radar platform movement, the sea clutter spectrum will generate a Doppler shift. Therefore, the sea clutter power spectrum is also referred to as the Doppler power spectrum, or more tersely, the Doppler spectrum [12]. The Doppler spectrum of sea clutter refers to the Fourier transform of the autocorrelation function of a continuous coherent time series signal within a single range gate on the sea surface. Different spectrum models correspond to different spectrum parameters, among which the most important are the Doppler shift and Doppler broadening. The former reflects the velocity of the sea surface scatterer motion, while the latter reflects the randomness of the scatterer motion. The spectrum characteristics of sea clutter can reflect the energy characteristics and motion phase information of the sea surface, playing an irreplaceable role in sea clutter research.

In the field of sea clutter spectrum foundational features, continuous research has been performed by Lamont-Smith et al. [13,14], who delved systematically and profoundly into the subject area. Under the precondition of considering Bragg and non-Bragg scattering mechanisms, the average spectral model of sea clutter has evolved from simplistic initial versions, such as the Gaussian model and power law model, to multi-component mixed models such as the Lee model [15], Walker model [16,17], Lamont-Smith model [18], and Rosenberg model [19,20]. The latter two models can be regarded as revisions of the Walker model. The China Research Institute of Radiowave Propagation [21,22] has established a time-varying Doppler spectrum model for sea clutter, addressing issues related to incomplete consideration of scattering mechanisms and inconsistencies between short-term and long-term modeling processes based on measured sea clutter data.

To enhance radar performance in detecting maritime targets, researchers have developed various effective sea clutter suppression algorithms, leveraging characteristics exhibited by sea clutter in the time and frequency domains. These algorithms significantly reduce the impact of sea clutter on target detection. Current approaches can be categorized into methods based on fractal and chaotic features of the sea surface [23,24], time-frequency analysis techniques [25,26], and artificial intelligence-based methods for detecting maritime targets [27,28].

The detection performance of radar systems is primarily influenced by the characteristics of sea clutter. Detection algorithms that utilize the spectral features of sea clutter aim to identify and suppress it, thereby improving target detection accuracy. According to optimal filtering theory, the optimal filter in a sea clutter background must adapt to variations in clutter characteristics. Given the inherent variability of sea clutter with environmental conditions, it is crucial to control the filter parameter changes based on real-time characteristics of the sea clutter to achieve adaptive optimal filtering. The improvement factor of the signal-to-clutter ratio (SCR) derived from the optimal filter is determined by

the spectral width of the clutter and the order of the filter. To obtain satisfactory detection performance, accurate estimation of sea clutter characteristics and real-time updates of filter coefficients are essential.

Based on the aforementioned analysis, understanding the backscattering characteristics and spectral properties of sea clutter can be achieved by obtaining sea surface state parameters within the radar detection area, such as ocean currents and waves. By leveraging these ocean dynamic parameters, the variations in filter parameters can be controlled, enabling the design of an optimal filter.

To obtain wind speed and direction information for a specific sea area at a particular time within the radar illumination region, various numerical models are commonly employed. Global meteorological models, such as the ECMWF (European Centre for Medium-Range Weather Forecasts) and GFS (Global Forecast System), are among the most frequently used options. However, global models often exhibit insufficient resolution for fine-scale predictions in localized areas. Wave models, such as WAM (Wave Mode) and SWAN (Simulating Waves Nearshore), are primarily designed for wave forecasting but can also indirectly provide information on wind speed and direction. WAM [29] is one of the most commonly used global wave models, being suitable for wave predictions in oceanic and coastal regions. In contrast, SWAN [30] is a local wave simulation tool focused on nearshore and shallow water applications, featuring high-resolution and flexible simulation capabilities. However, since predicting the wind field is not the primary objective of wave models, the accuracy of wind speed and direction forecasts is generally inferior to that of specialized meteorological models.

In comparison, the regional model WRF (Weather Research and Forecasting) model demonstrates clear advantages in localized forecasting. The WRF is a flexible, high-resolution regional meteorological model that allows users to define the simulation area and temporal scale according to their requirements [31]. It can achieve high-resolution forecasts through nested techniques and can be adjusted based on specific topographical and meteorological conditions, resulting in a simulation accuracy that significantly exceeds that of global models in particular regions. Especially in complex terrain or marine conditions, the WRF can capture more local details, such as land–sea breezes and localized wind field variations. Due to its flexibility, adjustability, and high resolution, the WRF provides distinct advantages in simulating wind speed and direction in localized sea areas. Compared to global and wave models, the WRF not only offers finer spatial resolution but also optimizes local forecasting accuracy through parameter adjustments and boundary condition modifications. Consequently, the WRF is a highly effective tool for short- and medium-term wind speed and direction predictions in specific marine areas. With the advancement of WRF versions, the WRF model is increasingly employed for high-precision regional wind field simulations [32–35].

After obtaining the ocean dynamical parameters, it is essential to design a filter that matches the spectral characteristics of sea clutter, employing matched filtering to suppress the clutter. The design of the filter is a critical step in this process. Digital filters, as effective signal processing tools, can suppress clutter with minimal distortion, making them widely used in radar signal processing systems. Digital filters are primarily categorized into Finite Impulse Response (FIR) filters and Infinite Impulse Response (IIR) filters [36]. FIR filters are renowned for their linear phase characteristics and stability, ensuring that the signal does not undergo phase distortion during filtering, which makes them particularly suitable for applications with high phase fidelity requirements. Despite their higher computational complexity, FIR filters can effectively preserve the original form of the signal in sea clutter removal, avoiding stability issues associated with feedback. In contrast, IIR filters utilize feedback loops to achieve greater computational efficiency. While they can provide similar

filtering effects at lower filter orders, their nonlinear phase characteristics and potential instability limit their application in high-precision scenarios.

This paper addresses the challenges of modeling the time-varying Doppler spectrum of sea clutter, the difficulty in obtaining real-time ocean dynamic parameters in radar detection areas, and the design of optimal filters for sea clutter Doppler spectra. We introduce the WRF meteorological model into the estimation of the sea clutter Doppler spectrum, replacing the previous ocean data inversion methods based on sea clutter data. By designing a parameterization scheme for the WRF model, we achieve fine-scale temporal and spatial simulations of ocean dynamic parameters such as wind speed and direction within the radar detection area. Subsequently, we estimate the sea clutter Doppler spectrum using empirical formulas based on the ocean dynamic parameters. With the estimated Doppler spectrum parameters, we employ FIR digital filters to accurately suppress clutter, ultimately enhancing the SCR improvement factor and improving radar target detection capabilities.

The main contributions of this paper are as follows:

1. The WRF meteorological model is introduced into the simulation of ocean parameters within a radar detection area. The parameterization scheme of the WRF model is calibrated using measured hydrological data from the radar detection area, ensuring simulation accuracy. This WRF numerical model simulation addresses the inability to grasp real-time changes in the ocean environment characteristics within the radar detection area.
2. Based on the simulated ocean dynamic parameters and integrating various sea clutter spectral computation methods, we develop a sea clutter spectrum estimation method based on ocean dynamic parameters. This enables the use of the WRF numerical model to investigate ocean environment parameters and subsequently estimate the sea clutter Doppler spectrum.
3. Utilizing the sea clutter Doppler spectrum parameters obtained from ocean dynamic parameter simulations, we design digital filters that match the spectral characteristics of sea clutter. By controlling the filter parameter changes based on simulated real-time sea clutter characteristics, we achieve adaptive optimal filtering, accurately suppressing clutter in radar echoes. The combination of ocean numerical modeling, ocean dynamics, and matched digital filters provides new insights for the development of sea clutter suppression technologies.

The remainder of this paper is organized as follows. Section 2 introduces the sea clutter suppression method based on ocean dynamics used in this paper. It incorporates the WRF numerical model to simulate ocean dynamic parameters, derives the calculation formula for the sea clutter spectrum, and analyzes the FIR digital filter. Finally, it introduces the two measured sea clutter datasets used in this study. Section 3 simulates various ocean dynamic parameters in the detection area based on the radar deployment location and gaze direction from the measured sea clutter data, comparing them with publicly available hydrological data for validation. We design digital filters for clutter suppression based on the sea clutter spectra and analyze the suppression effects, calculating the improvement factors at different target frequencies. Section 4 summarizes the paper and proposes future research plans.

2. Methods

This section primarily introduces the WRF model. Based on the WRF model and the methodology outlined in this section, the sea clutter suppression method driven by ocean dynamics is shown in Figure 1. The specific process is as follows: The WPS module of the WRF model is driven by terrain and gridded meteorological data matching the radar detection range. The WPS module consists of three main steps: its geogrid interpolates

static geographical data onto the model grid, its ungrid extracts meteorological field data from GRIB-format driver files, and its metgrid horizontally interpolates the meteorological field data extracted by ungrid onto the simulation domain grid defined by geogrid. Upon completion of WPS preprocessing, the WRF model performs simulation, outputting oceanic dynamic parameters such as wind speed and direction at specific distance units along radar gaze directions. During WRF model simulation, parameterization schemes are calibrated against meteorological data measured by buoys within the radar detection region, selecting the optimal parameterization scheme that matches the sea area. Based on oceanic dynamic parameters simulated by the WRF model, the power spectrum of sea clutter is estimated using empirical formulas. Corresponding sea clutter suppression filters are designed based on the sea clutter power spectrum to suppress sea clutter signals in radar returns.

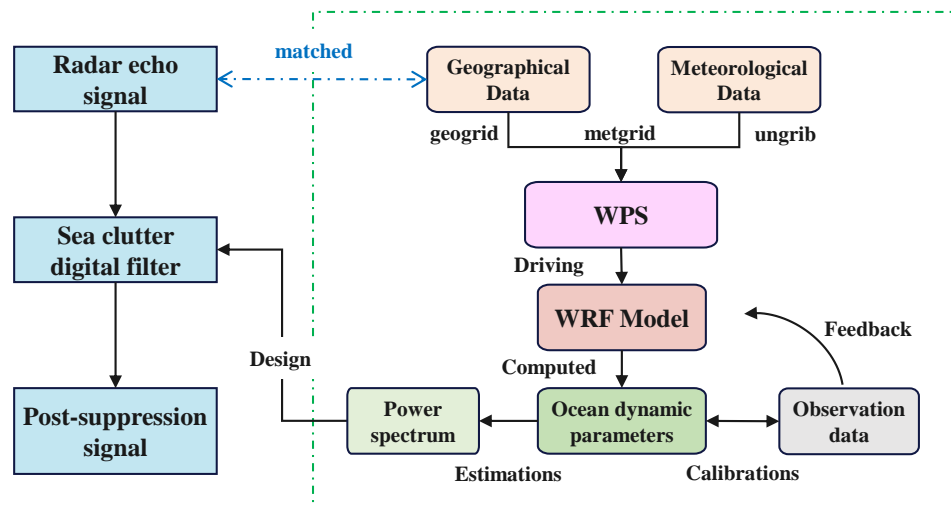


Figure 1. Block diagram of sea clutter suppression based on ocean dynamics.

2.1. Simulation of Ocean Dynamics Parameters Based on the WRF Model

The WRF model is based on the fully compressible, non-hydrostatic Euler equations in the flux form, allowing bidirectional and unidirectional multilayer nested domains on horizontal grids. It employs the Arakawa C grid for the horizontal grid format and an improved σ -coordinate for vertical direction (terrain-following η -coordinate). The WRF model allows vertical stratification in three-dimensional space and is adaptable to various research configurations, thereby mitigating significant errors inherent in calculating advection terms, horizontal pressure gradient forces, and horizontal diffusion terms over steep terrain coordinates. This atmospheric dynamics framework incorporates state-of-the-art dynamic and physical processes, facilitating the selection and configuration of different parameterization schemes according to research needs. This capability ensures the model’s applicability across diverse spatial and temporal scales, thereby enhancing numerical simulation outcomes.

The vertical coordinate system of the WRF model follows the terrain with a static pressure-based η -coordinate [37]:

$$\eta = (p_h - p_{ht}) / \mu \tag{1}$$

where p_h represents the hydrostatic portion of atmospheric pressure, $\mu = p_{hs} - p_{ht}$, and p_{ht} and p_{hs} denote the atmospheric pressure at the upper and lower boundaries (ground surface) of the numerical model, respectively. $\eta = 0$ indicates the upper boundary, while $\eta = 1$ represents the lower boundary.

This η coordinate is also known as the terrain-following height coordinate. $\mu(x, y)$ represents the unit area mass of the entire atmospheric layer at any point within the region,

which varies with the horizontal grid position. Therefore, the flux form expression for atmospheric variables is given by

$$V = \mu(u, v, w) = (U, V, W), \Omega = \mu\dot{\eta}, \Theta = \mu\theta \tag{2}$$

where $w = \eta$, (u, v, w) represents the covariant velocity components in the vertical and horizontal directions, and θ represents potential temperature.

Using the newly defined variables described above, we introduce potential height $\phi = gz$, atmospheric pressure p , and the reciprocal of air density $\alpha = 1/\rho$ as three nonconservative variables. The flux form of the Euler equations is then rewritten as follows:

$$\frac{\partial U}{\partial t} + (\nabla \cdot Vu) - \frac{\partial}{\partial x} \left(p \frac{\partial \phi}{\partial \eta} \right) + \frac{\partial}{\partial \eta} \left(p \frac{\partial \phi}{\partial x} \right) = F_U \tag{3}$$

$$\frac{\partial V}{\partial t} + (\nabla \cdot Vu) - \frac{\partial}{\partial y} \left(p \frac{\partial \phi}{\partial \eta} \right) + \frac{\partial}{\partial \eta} \left(p \frac{\partial \phi}{\partial y} \right) = F_V \tag{4}$$

$$\frac{\partial W}{\partial t} + (\nabla \cdot Vw) - g \left(\frac{\partial p}{\partial \eta} - \mu \right) = F_W \tag{5}$$

$$\frac{\partial \Theta}{\partial t} + (\nabla \cdot Vw) = F_\Theta \tag{6}$$

$$\frac{\partial \mu}{\partial t} + (\nabla \cdot V) = 0 \tag{7}$$

$$\frac{\partial \phi}{\partial t} + \frac{1}{\mu} [(\nabla \cdot \nabla \phi) - gW] = 0 \tag{8}$$

Additionally, the expression for the reciprocal of density α in the hydrostatic equilibrium equation is given by

$$\frac{\partial \phi}{\partial \eta} = -\alpha\mu \tag{9}$$

The equation of state is as follows:

$$p = p_0(R_d\theta/p_0\alpha)^\gamma \tag{10}$$

In Equations (3)–(10), assuming a represents a general variable, we have the following:

$$\nabla \cdot Va = \frac{\partial}{\partial x}(Ua) + \frac{\partial}{\partial y}(Va) + \frac{\partial}{\partial \eta}(\Omega a) \tag{11}$$

$$\nabla \cdot Va = U \frac{\partial a}{\partial x} + V \frac{\partial a}{\partial y} + \Omega \frac{\partial a}{\partial \eta} \tag{12}$$

In Equations (3)–(10), F_Θ , F_V , F_U , and F_W denote forcing terms due to Earth’s rotation, turbulent mixing, model physical processes, and spherical projection, respectively; p_0 is the reference pressure (typically 10^5 pascals), R_d is the gas constant for dry air; $\gamma = C_p/C_v = 1.4$, where C_p denotes the specific heat capacity at constant pressure; and C_v represents the specific heat capacity at constant volume.

2.2. Sea Clutter Spectrum Estimation Based on Ocean Dynamics Parameters

Sea clutter is influenced not only by the swell structure of the sea surface but also by local gusts and scattering mechanisms. Despite such complex relationships, empirical formulas for the Doppler shift and spectral width of sea clutter can be derived. The time scale of concern for modeling the average spectral shape of sea clutter is generally on the order of seconds or more to ensure that the observed data can cover at least one complete period of a gravity wave [38]. The average Doppler shift is a function of the wind speed,

and it is proportional to the cosine of the angle between the wind direction and the radar detection direction [39], as shown in the following equation:

$$f_D = \frac{2\cos\phi\cos\theta_g}{\lambda}(v_w \pm v_c \pm c_p) \tag{13}$$

where θ_g is the grazing angle, λ is the microwave wavelength, and v_w , v_c , and c_p refer to wind drift, current velocity, and the speed of the scattering object on the water surface, respectively. ϕ is the angle between the wind direction and the radar detection direction.

Equation (13) neglects the surface tilt and vertical motion, instead approximately calculating the sea clutter spectrum. The plus and minus signs, respectively, correspond to the contributions of the approaching or receding scatterers. c_p is calculated based on the following equation:

$$c_p = \left(\frac{g}{k_w} + \frac{\gamma}{\rho}k_w\right)^{1/2} \tag{14}$$

where g is the gravitational acceleration, γ and ρ are the water surface tension and density, respectively, and k_w is the associated wave number. Generally, $\gamma = 0.078$ N/m, and $\rho = 1026$ kg/m³. For Bragg scattering,

$$k_w = \frac{4\pi\cos\theta_g}{\lambda} \tag{15}$$

The calculation equation for the grazing angle θ_g is as follows [40]:

$$\theta_g = \arcsin\left(\frac{h}{R} + \frac{h^2}{2r_e R} - \frac{R}{2r_e}\right) \tag{16}$$

where h denotes the height of the radar, r_e is the radius of the Earth, and R represents the distance from the radar to the target, which can be obtained from the distance unit of the measured data.

According to the measured data and theoretical derivation [41,42], when the grazing angle is less than 45 degrees, the calculation of the average velocity of the sea clutter Doppler spectrum can be simplified to the following equation:

$$\begin{aligned} V_{HH} &= (0.25 + 0.18U + 0.07U\cos(2\theta_g))\cos\theta_g \\ V_{VV} &= (0.25 + 0.18U)\cos\theta_g \end{aligned} \tag{17}$$

where HH indicates that the radar transmits and receives electromagnetic waves with horizontal polarization, and VV indicates that the radar transmits and receives electromagnetic waves with vertical polarization.

The antenna beamwidth causes broadening of the sea clutter spectrum, known as the Doppler spectrum width, which can be expressed as follows:

$$\Delta f_D = \frac{2V}{\lambda}(\cos\psi_2 - \cos\psi_1)\cos\phi \tag{18}$$

where ψ_1 and ψ_2 are the local grazing angles at the front and rear boundary points of the illuminated area, respectively.

2.3. FIR Filter Design

FIR filters are a class of digital filters whose output depends solely on a linear combination of the input signal. The design of FIR filters is highly flexible, allowing coefficients to be precisely adjusted as needed, which ensures good stability and eliminates feedback issues. Consequently, FIR filters are widely used in digital signal processing, particularly

in applications requiring precise phase accuracy and stable signals, enabling effective processing and suppression of interference within signals. The output formula for an FIR filter is given by

$$y[n] = \sum_{k=0}^{N-1} h[k]x[n-k] \quad (19)$$

where $y[n]$ is the output signal at time n , $x[n-k]$ represents the current and previous k values of the input signal, $h[k]$ denotes the filter's impulse response or coefficients, and N indicates the order of the filter, representing the length of the impulse response.

The structure of FIR filters ensures that the output depends exclusively on the input signal, thus avoiding feedback loops, which guarantees that the filter remains stable. Additionally, the finite length of the FIR filter's impulse response means that its output will eventually return to zero after a finite number of input values. In the frequency domain, the frequency response of an FIR filter is expressed as

$$H(e^{j\omega}) = \sum_{k=0}^{N-1} h[k]e^{-j\omega k} \quad (20)$$

where $H(e^{j\omega})$ represents the frequency response of the filter, and ω is the normalized angular frequency.

The frequency response allows for the analysis of the impact of FIR filters on different frequency components of a signal. An important characteristic of FIR filters is the ability to design them as linear phase filters, which ensures that all frequency components experience the same phase delay, thereby preserving the integrity of the signal's phase. Another notable advantage of FIR filters is their inherent stability, as the absence of feedback structures guarantees stability regardless of the chosen filter coefficients. FIR filters facilitate the realization of arbitrary amplitude responses and allow for effective control over the filtering effects across different frequency ranges.

2.4. The Measured Sea Clutter Dataset

Due to the ever-changing nature of the marine environment, sea clutter exhibits complexities in both temporal and spatial dimensions, rendering simulated sea clutter data inadequate in capturing its actual characteristics. Therefore, empirical data are typically employed in practical research on sea clutter. This subsection introduces the measured sea clutter data collected from the X-band radar and IPIX radar datasets, including the spatial-temporal distribution and spectral variation plots, providing measured data for the subsequent simulation of sea clutter spectra and sea clutter suppression.

2.4.1. X-Band Radar Dataset

The X-band radar measured sea clutter dataset is derived from the "Sea-detecting X-band Radar and Data Acquisition Program". The X-band radar is located on Yangma Island in Yantai, a northern city in China, approximately 50 m inland from the coastline and at an elevation of about 30 m above sea level. The radar has a field of view of approximately 180°, and data were collected under sea state conditions ranging from levels 1 to 4. The specific coordinates of the radar are 121°36.7' E and 37°28.35' N, as illustrated in Figure 2.

The radar operates in the X-band with a frequency range of 9.3–9.5 GHz, using HH polarization, a pulse width of 40 ns, a pulse repetition frequency (PRF) of 3000 Hz, and a range resolution of 6 m. The grazing angle range for significant sea clutter data is approximately 0.3° to 15°. The X-band radar data selected for this paper are from the first quarter of 2019. The range-pulse diagram of this data is shown in Figure 3.



(a)



(b)

Figure 2. Schematic of the X-band radar. (a) The placement of the X-band radar. (b) Actual photograph of the X-band radar.

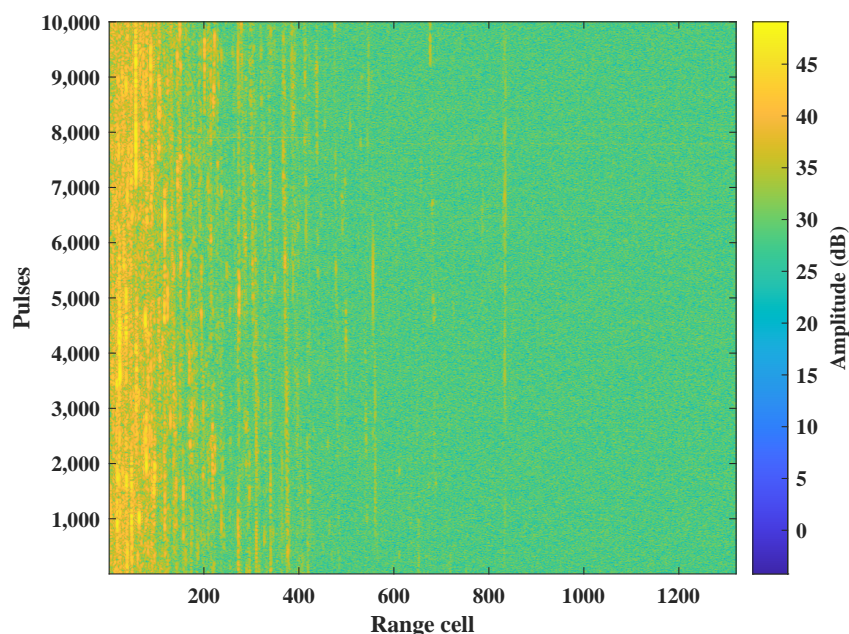


Figure 3. Range–pulse distribution of the X-band radar data.

2.4.2. IPIX Radar Dataset

The IPIX radar dataset is a large database obtained by McMaster University in Canada in 1993 and 1998 using the IPIX radar, which was installed on a cliff 30 m above sea level. The radar was directed toward the Atlantic Ocean, and the target to be detected was a floating sphere with a diameter of 1 m wrapped in aluminum wire. The radar beam width was 0.9° , and the range resolution was 30 m. The radar operated in a dwell mode, with each data file containing 14 range cells, each with 131,072 sampling points, and a dwell time of approximately 131 s. The IPIX radar can transmit both horizontally and vertically polarized electromagnetic waves and can utilize two linear receivers to achieve horizontal and vertical reception. Therefore, during data acquisition, the radar typically obtained HH, VV, HV, and VH types of polarized radar echo data. This paper employs data from 1993,

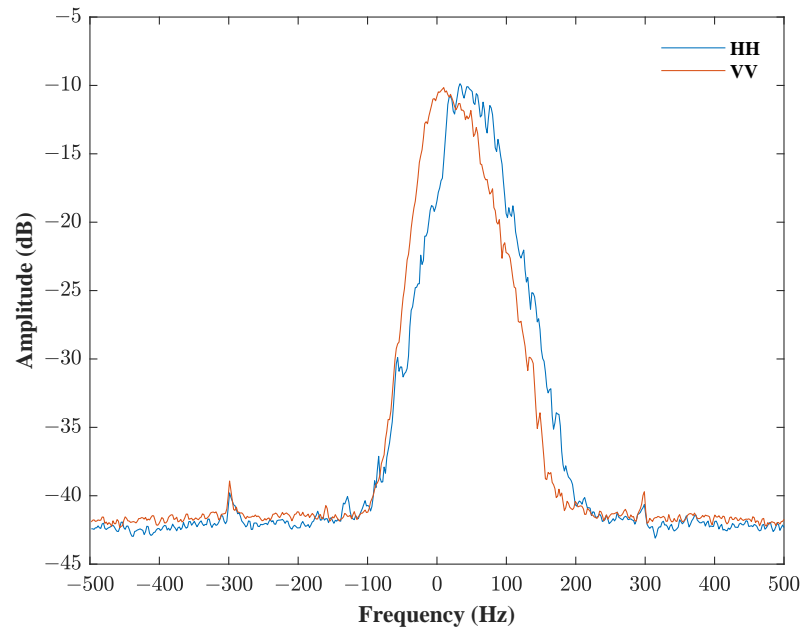


Figure 6. Doppler spectrum of IPIX measured sea clutter data.

When analyzing the time-varying characteristics of sea clutter spectrum, it is important to select an appropriate time segment. If the duration of the data segment is less than the gravity wave period, the local power level of the sea clutter remains approximately constant, and the sea clutter can be regarded as a quasi-stationary random signal. Therefore, when segmenting the data, the correlation time of the sea clutter data must be considered, along with the length of each data segment to enhance the spectral estimation resolution. The IPIX radar #40 dataset, totaling 131 s, was used with HH polarization to plot the Doppler variation over time, as shown in Figure 7. Figure 7 demonstrates that the Doppler frequency of the sea clutter continuously changed over time.

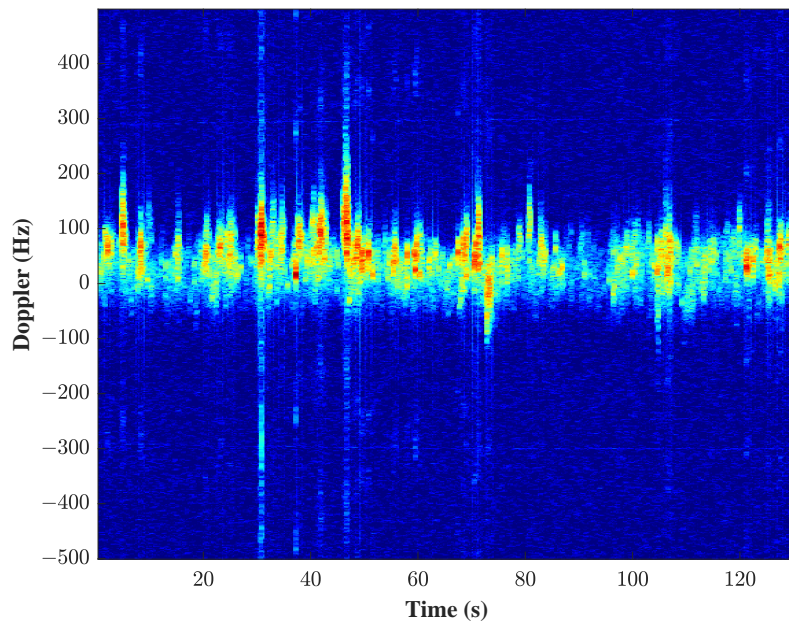


Figure 7. Time–Doppler diagram of sea clutter.

3. Results and Discussion

In this section, we discuss how the WRF model was used to simulate the ocean dynamic parameters within the radar detection area, such as wind speed and wind direction,

and these simulations were then compared and validated against measured data. Subsequently, the sea clutter power spectrum was estimated based on the equations, digital filters were designed to suppress the sea clutter, and the suppression effects were analyzed.

3.1. WRF Model Simulation Results

The WRF model utilizes the WRF-ARW (Advanced Research WRF), version 4.3, operating on the Linux operating system. The basic parameter settings of the WRF model are depicted in Table 1.

Table 1. Basic parameter configuration scheme of WRF model.

Options	Parameter
Geogrid	D01: 172 × 127 (3 km) D02: 151 × 118 (1 km) D03: 229 × 175 (0.3 km)
IC BC	ERA5 1-h 0.25 deg feedback = 1
Domains	dt = 15 s grid_ratio = 3 time_step_ratio = 3 smooth_option = 0
Dynamics	hybrid_opt = 2 w_damping = 0
Physics	mp_physics: WSM6 cu_physics: Kain-Fritsch (new Eta) (D01, D02), off (D03) ra_lw_physics: RRTMG ra_sw_physics: RRTMG sf_surface_physics: unified Noah land-surface model

The model employs a three-layer nested grid configuration, with the finely nested third layer primarily covering the radar detection area. The grid resolution-to-time ratio in the WRF model was set to 3, ensuring optimal spatial and temporal resolution. Initial and boundary conditions were initialized using ERA5 data [44], ensuring reliable inputs for meteorological simulations. ERA5 is the fifth generation ECMWF reanalysis for the global climate, with a temporal resolution of 1h and a spatial resolution of 0.25° for the WRF model. In most cases of WRF model simulations, the choices of grid size and integration step depend on the scale of the experiment, available computational resources, and other factors. In this paper, the grid size was primarily selected based on the radar resolution, while the integration time was set to five times the grid size, measured in kilometers, as recommended on the official WRF website. According to the WRF guidelines, when the grid size is less than 4 km, the impact of the cumulus parameterization scheme is relatively small. Therefore, in the sensitivity experiments conducted in this paper, the focus was mainly on the microphysics schemes, with the WSM6, WDM6, and Thompson schemes selected for comparison [45]. The Taylor diagram [46] of the parameterization results for the three different microphysics schemes is shown in Figure 8, with the WSM6 scheme, which exhibited the highest accuracy, ultimately selected. For the other parameterization schemes, the high-precision schemes available in the WRF version were chosen.

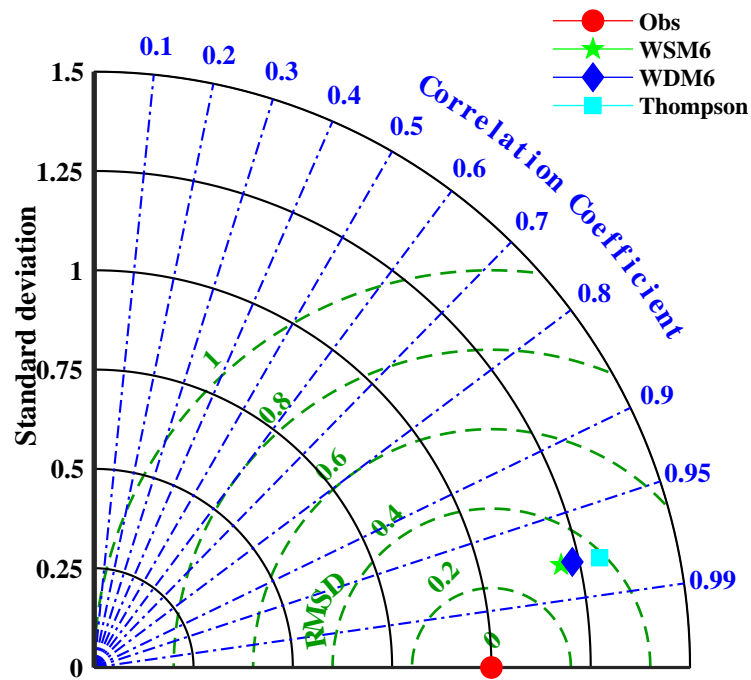


Figure 8. Taylor diagram of the parameterization results for different mp_physics schemes.

Based on the publicly available X-band radar dataset [47], the computational area for this paper was set in the northern Yellow Sea, with a longitude range of 117° E to 123° E and a latitude range of 36.2° N to 39.8° N. The computational area is shown in Figure 9. The radar station is situated on Yangma Island in Yantai City. The red rectangle represents the third nested grid of the WRF model, where the location of the X-band radar on Yangma Island is indicated by a red upward triangle with coordinates of 121°36.7' E and 37°28.35' N.

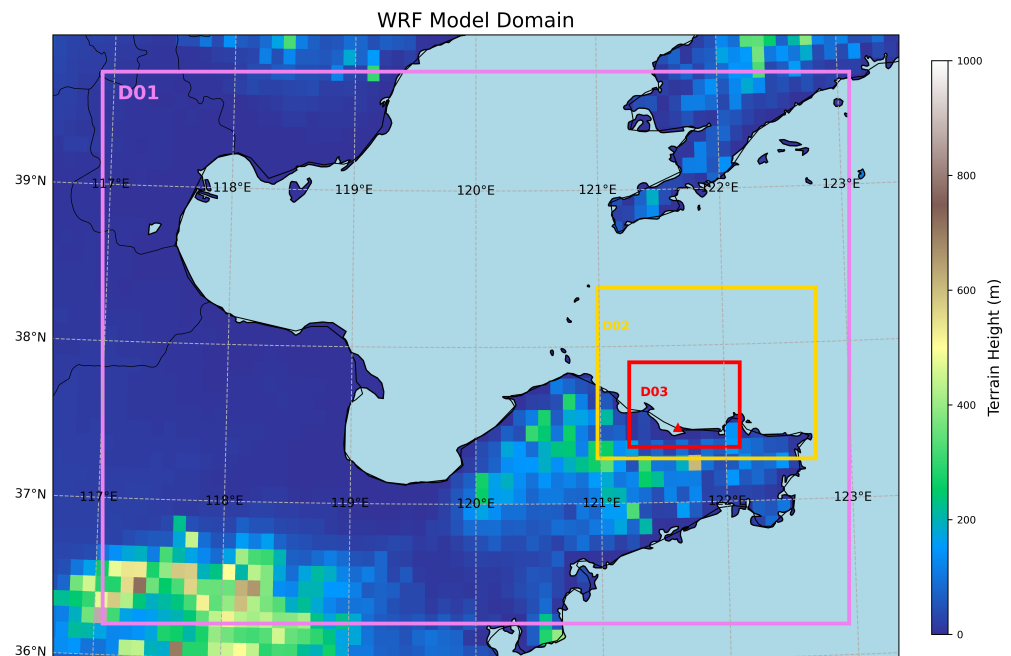


Figure 9. Simulation of WRF model grid over the X-band radar detection area. The red upward triangle indicates the radar installation location.

The WRF model was employed to simulate ocean dynamic parameters in the IPIX radar detection area located on the Dartmouth coast in Canada, with the WRF grid configuration depicted in Figure 10.

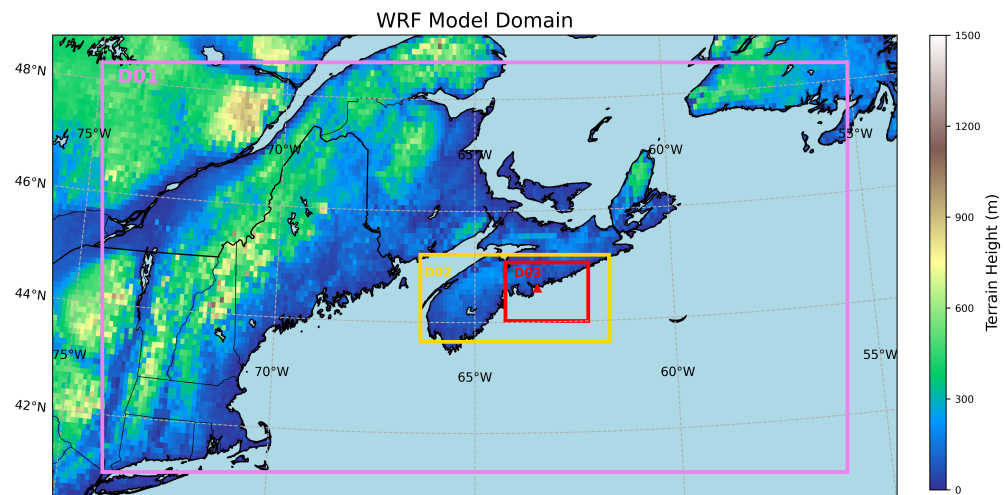


Figure 10. The WRF model grid over the IPIX radar detection area. The red upward triangle indicates the radar installation location.

The simulated region spans longitudinally from 55° W to 75° W and latitudinally from 41° N to 48° N. The red rectangular area represents the third-layer nested grid, covering the radar's detection range, with a red triangle indicating the IPIX radar located at 44.612° N, 63.4235° W. This paper utilized the IPIX dataset, specifically dataset #40, to simulate ocean dynamic parameters. Radar measurements were taken at 00:00 on 10 November 1993. Recorded meteorological data include a wind direction of 200°, wind speed of 2.5 m/s, temperature of 6.5 °C, and relative humidity of 87%.

Taking the X-band radar dataset as an example, this study validated the accuracy of oceanic dynamic parameters simulated by the WRF model. After setting the research area and the driving files for the WRF model, the wind speed and wind direction at a certain point in the X-band radar detection area were simulated. The simulation time was from 0:00 on 12 October 2019 to 0:00 on 13 October 2019, and the results were output every 30 min for a total of 49 datasets. The parametrization scheme was adjusted according to publicly available sea state data parameters. The simulation results are shown in Figure 11. The Mean Squared Error (MSE) of the wind speed obtained from WRF simulations compared to the measured data came out to 0.0614, the Root Mean Squared Error (RMSE) came out to 0.2478, the Mean Absolute Error (MAE) came out to 0.2117, and the coefficient of determination (R^2) came out to 0.8679. For wind direction, the MSE came out to 10.0536, the RMSE came out to 3.1707, the MAE came out to 2.8445, and the R^2 came out to 0.8636. The results from the WRF simulations closely align with the measured data.

3.2. Simulation Results of Sea Clutter Spectrum

The X-band radar measured data selected the 20191012112446 staring data, with the first sampling point at a distance of 0.0775 km. The antenna polarization was HH polarization. The temporal dimension comprised 10,000 groups. The 500th distance unit was selected for the distance dimension, corresponding to a latitude and longitude of 37.48437° N and 121.6134° E at the radar detection point. The radar grazing angle was calculated to be 3.45° using Equation (16). According to the WRF model simulation, the angle ϕ between the wave direction at the radar detection point and the radar azimuth was found to be 57°, with a wind speed of 3.257 m/s. Substituting these parameters into the sea clutter spectrum estimation equation, the Doppler frequency was estimated to be 30.82 Hz. The power spectrum obtained from the measured data is plotted in Figure 12, indicating a peak frequency of 29.29 Hz.

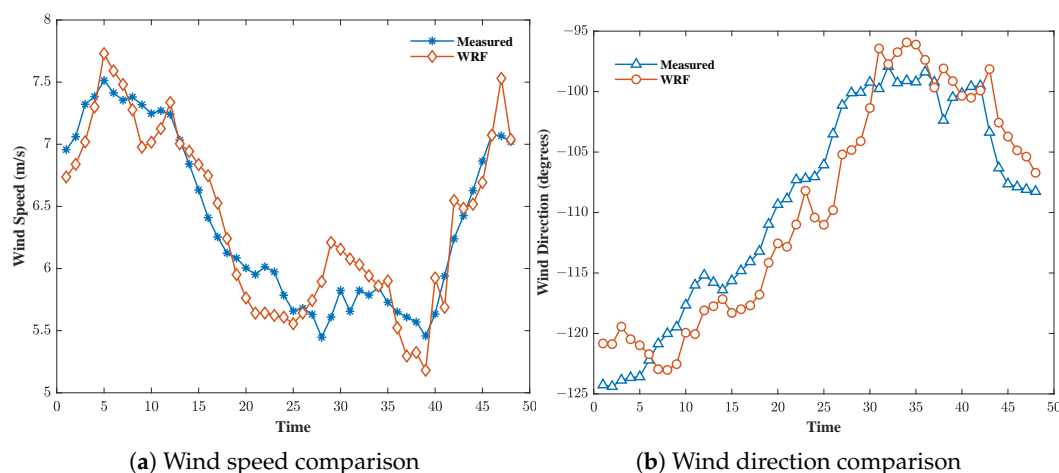


Figure 11. Comparison of ocean dynamic parameters obtained from WRF simulations with measured data.

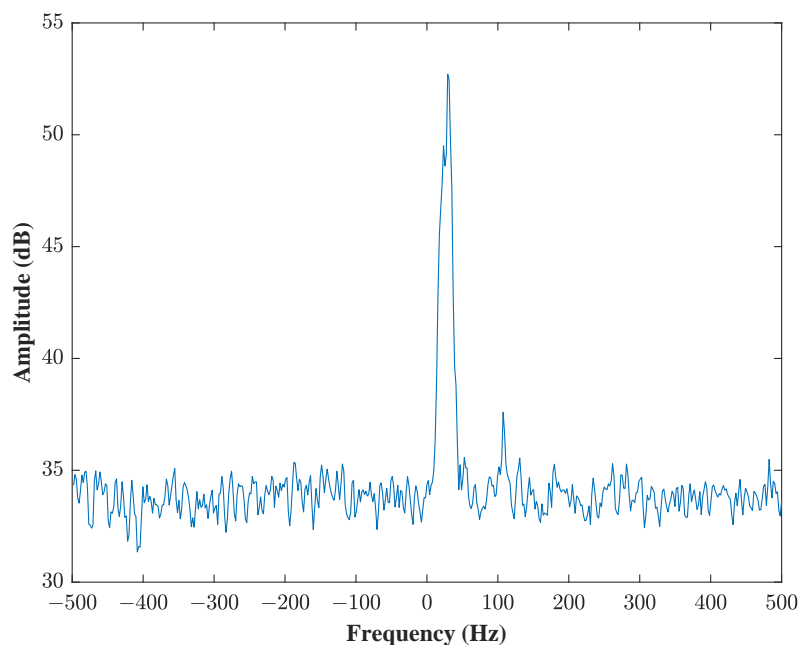


Figure 12. Measured power spectrum of pure clutter signal.

In the estimation of sea surface radar echo Doppler spectra, both numerical model calculations of ocean parameters and direct radar data-based sea clutter spectrum estimation have their respective advantages and limitations. The WRF numerical model used in this study can accurately estimate the spatiotemporal variations of sea clutter by simulating factors such as wind speed, wave patterns, and meteorological conditions in the ocean environment. This approach not only accounts for the coupling effects of multiple physical fields but also provides more precise sea surface echo predictions than actual radar observations, especially in the absence of in situ radar data. Furthermore, the numerical model can perform sensitivity experiments and scenario simulations to predict sea surface radar echoes under different meteorological and oceanic conditions, offering more comprehensive theoretical support for sea surface detection. In contrast, directly estimating the sea clutter spectrum from radar data offers the advantage of real-time application and on-site observation. Radar data provide high spatiotemporal resolution and directly reflects changes in the sea surface environment. However, this method also has certain limitations. Radar echo data are prone to noise and environmental interference, especially under adverse weather conditions and complex sea states, which can degrade the quality of

the signal. Additionally, the radar-based sea clutter spectrum is constrained by the radar’s range and positioning, potentially failing to capture all dynamic variations in complex environments. Therefore, in practical applications, the combination of numerical models and radar data can complement each other’s shortcomings, providing more accurate and reliable sea surface radar echo spectrum predictions.

3.3. Algorithmic Complexity

In terms of algorithmic time complexity, the FIR filter requires multiplication of the most recent N input signal values with their corresponding filter coefficients for each output sample, followed by the summation of these products. Therefore, the computational complexity for each output sample is $O(N)$. If there are a total of M output samples, the overall time complexity becomes $O(M \cdot N)$. Regarding space complexity, the FIR filter must store N filter coefficients, the most recent input signal values, and the output signal, resulting in a space complexity of $O(M + N)$. Since both the order of the FIR filter and the number of output samples are considered constants, the algorithmic complexity for sea clutter suppression based on the FIR digital filter is regarded as constant, making it efficient due to its low complexity.

In the WRF model, the spatial computational complexity is primarily related to the model’s grid resolution; higher spatial resolution significantly increases the number of computational cells, leading to complexity growth in the form of $O(n^2)$, where n is the number of grid points. Additionally, increasing the number of vertical layers linearly enhances the computational load, resulting in an overall complexity that can be expressed as $O(n^2 \cdot m)$, where m represents the number of vertical layers. In terms of time complexity, the computational burden of the model is closely tied to the time step; smaller time steps lead to frequent computational updates, significantly increasing runtime. Overall, the computational complexity of the WRF model during ocean parameter simulation is contingent upon the selection of spatial and temporal parameters, with higher time and spatial resolutions resulting in greater computational complexity.

3.4. Analysis of Sea Clutter Suppression Results

The amplitude and phase responses of the FIR filter designed based on the power spectrum of the measured data are shown in Figure 13. The blue line represents the amplitude response, and the orange line represents the phase response.

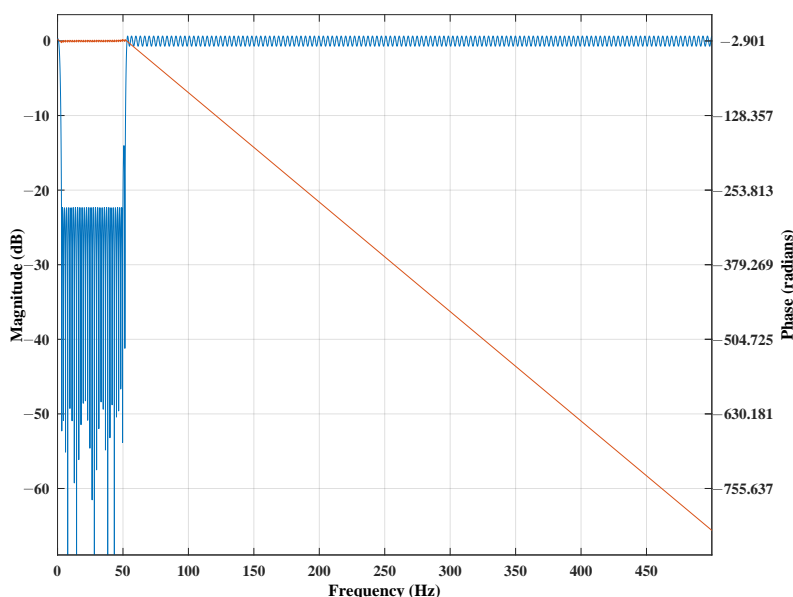


Figure 13. Magnitude and phase responses of the FIR filter.

The design of the FIR filter is directly influenced by the oceanic parameters simulated by the WRF model. Oceanic dynamic parameters, such as wind speed and wind direction, are crucial for characterizing the Doppler spectrum. The selection of different meteorological models and parameterization schemes significantly affects the accuracy of sea surface echo predictions, which in turn impacts the filter design. Variations in the predicted oceanic parameters can alter the spectral distribution and power spectral density of the Doppler spectrum, directly influencing the design of the FIR filter, including the cutoff frequency and filter order. Therefore, the accuracy of the meteorological model plays a key role in the effectiveness of the filter, as inaccurate oceanic dynamic parameters may lead to suboptimal filtering performance. This further emphasizes the importance of model accuracy in ensuring precise sea surface echo predictions and optimizing filter design.

Wavelet transform and Empirical Mode Decomposition (EMD) reconstruction methods [48] are applied to suppress the #17 sea clutter data from the IPIX radar. The results are shown in Figure 14.

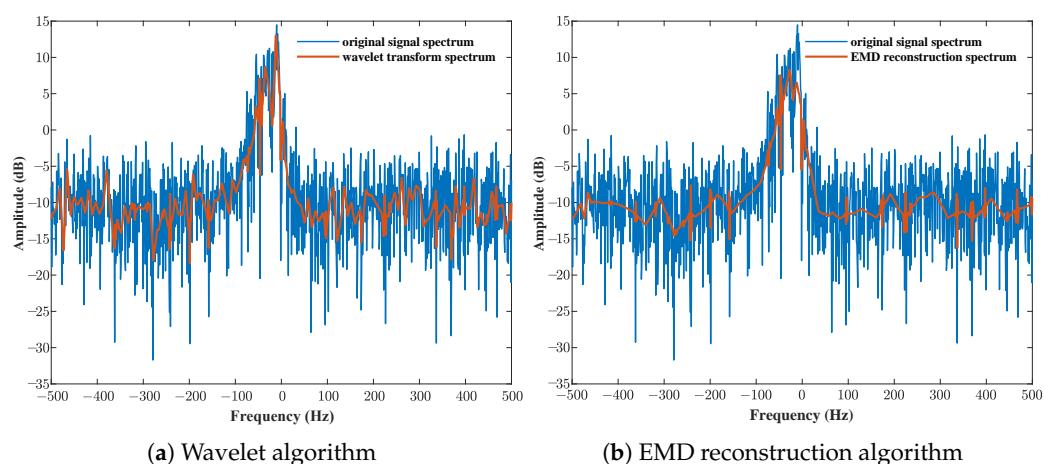


Figure 14. Wavelet and EMD reconstruction suppression algorithm. (a) Wavelet transform-weighted reconstruction. (b) EMD reconstruction.

In this paper, the db3 (Daubechies 3) wavelet was chosen as the wavelet basis for performing wavelet transform to process radar data after distance processing, beamforming, and Doppler processing. Assuming that the Doppler spectrum of the 0th range gate being processed is denoted as $RD(r_0, f_d)$, the wavelet transform with the db3 wavelet is applied to this spectrum, extracting the time–frequency features at different scales. Wavelet transform effectively captures local discontinuities and spectral variations within the signal, thereby revealing the complex dynamic characteristics of the target. Specifically, wavelet transform enables multi-scale analysis, decomposing the spectral signal into different frequency components, which helps in identifying key features within the Doppler spectrum. Subsequently, single-branch reconstruction and weighted merging are performed. For the EMD method, the Doppler signal $RD(r, f_d)$ is decomposed into multiple Intrinsic Mode Functions (IMFs) and a residual term. Each IMF represents a different frequency component of the signal and reflects changes in the signal at various time scales. By analyzing these IMFs, the target echo and clutter components of the signal can be effectively separated. Then, by selecting appropriate IMFs, noise and irrelevant components can be removed, enhancing the target signal and improving the radar system’s capability to recognize and track the target.

Traditional algorithms impose numerous constraints during signal reconstruction, often requiring the setting of various parameters. Consequently, they cannot accurately

identify clutter frequencies and can only partially denoise the echo signals, resulting in suboptimal suppression performance.

Two single-frequency simulated signals with frequencies of -100 Hz and 100 Hz, respectively, were added to the X-band radar measurement data of the 20191012112446 staring data. The amplitude of the simulated signals was set lower than that of the sea clutter. The power spectrum of the sea clutter, after suppression using the FIR filter, is shown in Figure 15. As illustrated in Figure 15, the sea clutter around 30 Hz was effectively suppressed, while the simulated signals at -100 Hz and 100 Hz were preserved.

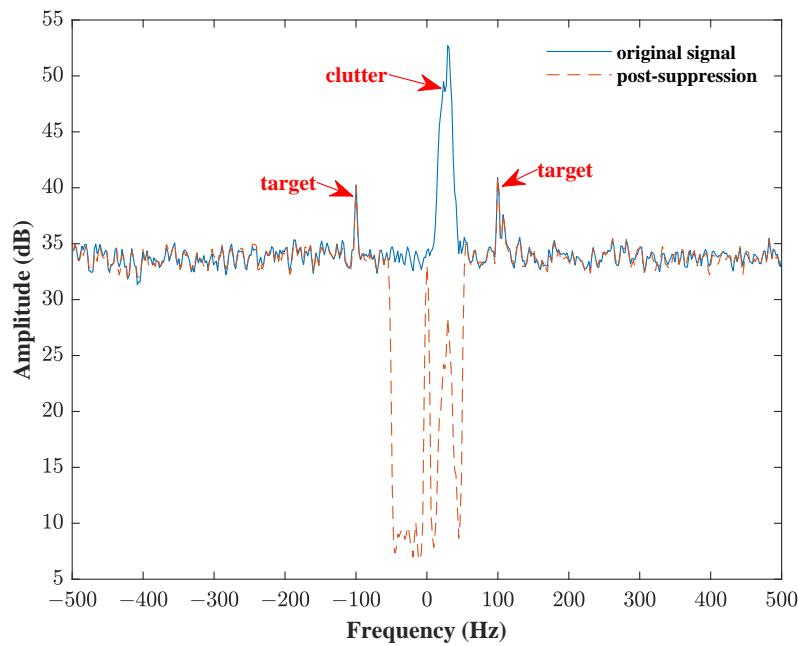


Figure 15. Power spectrum before and after sea clutter suppression.

After adding the target signals at -100 Hz and 100 Hz to the measured radar dataset, the radar range–Doppler (RD) diagrams before and after ocean dynamics suppression are plotted, as shown in Figure 16. The radar RD diagram converts the radar echo signal into a two-dimensional representation of the range and Doppler frequency, where the horizontal axis represents Doppler frequency and the vertical axis represents range cells. As seen in Figure 16a, the clutter Doppler frequency varies little within 50 range cells. From the suppressed diagram in Figure 16b, it can be observed that the clutter near zero frequency was mostly filtered out, while the two target signals at -100 Hz and 100 Hz were successfully retained.

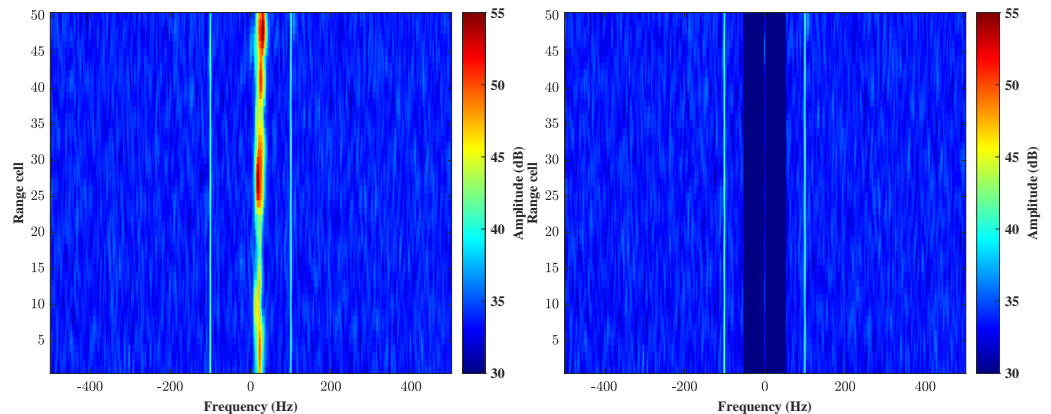
In radar systems, the improvement factor is defined as the ratio of the signal-to-clutter ratio at the output of the clutter filter to the signal-to-clutter ratio at the input. The equation for calculating the improvement factor is given as follows:

$$I = \frac{S_o / (C_o + N_o)}{S_i / (C_i + N_i)} \tag{21}$$

where I is the improvement factor, S_o is the output target signal power, C_o is the output clutter power, N_o is the output noise power, S_i is the input target signal power, C_i is the input clutter power, and N_i is the input noise power.

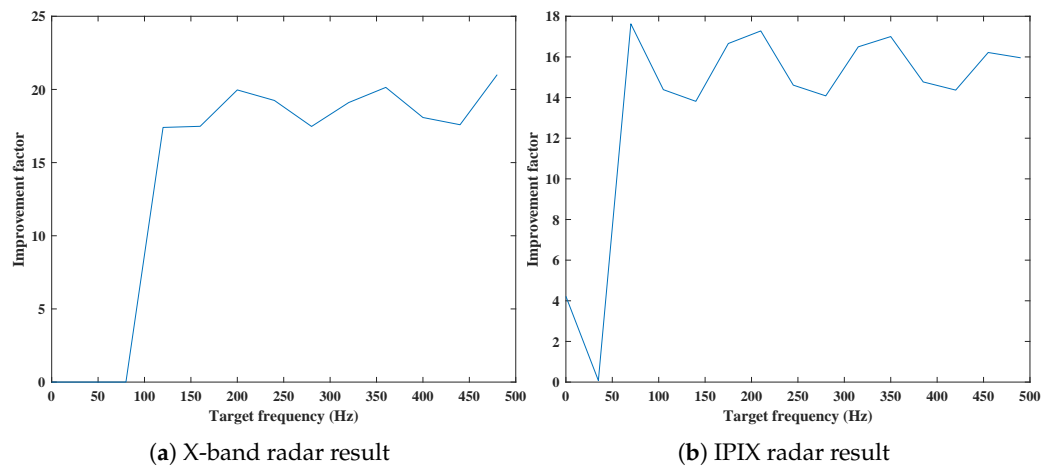
Simulated targets of different frequencies are added to the sea clutter, and the improvement factor of sea clutter suppression based on ocean dynamics is shown in Figure 17. As can be seen from Figure 17, filters at different target frequencies have certain improvement effects. In particular, when the target frequency lies outside the power spectrum of sea

clutter, the average improvement factor of the filter can reach 17.22, demonstrating the effectiveness of the proposed method in suppressing sea clutter.



(a) Range-Doppler diagram before suppression (b) Range-Doppler diagram after suppression

Figure 16. Range-Doppler diagrams of radar before and after sea clutter suppression.



(a) X-band radar result

(b) IPIX radar result

Figure 17. Correspondence between improvement factor and target signal frequency.

4. Conclusions

This paper analyzes the Doppler shift and broadening phenomenon caused by sea surface wave motion in the radar beam illuminating area. Building on the mechanisms of shore-based radar sea clutter spectrum and existing research on sea clutter spectrum characteristics, we proposed a sea clutter suppression method based on ocean dynamics. The WRF model was employed to simulate the marine parameters affecting the sea clutter spectrum in correlation with time and radar range units. Two sets of measured sea clutter data were used to suppress the sea clutter, and the suppression results were analyzed. The suppression results show that the sea clutter suppression based on the WRF model of ocean dynamics has a certain effect. Although the empirical formulas are data-dependent, this method provides a viable solution for sea clutter suppression technology. Given that the power spectrum estimation of sea clutter is based on empirical formulas, the spectrum width of sea clutter varies significantly, posing a challenge for future ocean dynamics-based suppression methods.

This paper utilized the WRF model to retrospectively simulate sea clutter spectrum based on existing oceanic parameters. In practical applications, the forecasting capabilities of the WRF model can be employed using global forecasting data such as the GFS to predict oceanic dynamic parameters, including wind speed and direction, for a specific radar

detection area over an upcoming period. This enables advanced simulation and suppression of sea clutter spectrum, thereby aiding in target detection under sea clutter conditions.

Sea clutter characteristic sensing is of great significance in the field of sea surface target detection, particularly in the current era of progressively advanced information technology. There is immense potential for further research in this area. Leveraging the strong fitting capabilities of deep learning, neural networks can be utilized to extract the relevant features between sea waves within the radar detection area to estimate the sea clutter spectrum, presenting a promising research direction.

Author Contributions: Conceptualization, G.L. and Y.C.; methodology, G.L. and X.M.; software, G.L. and Z.W.; validation, Y.C. and Z.W.; formal analysis, Y.C.; investigation, Z.W.; data curation, G.L.; writing—original draft preparation, G.L.; writing—review and editing, Y.C.; visualization, X.M.; supervision, Z.W.; project administration, H.Z.; funding acquisition, H.Z. All authors have read and agreed to the published version of the manuscript.

Funding: This research was supported by the Fundamental Research Funds for the Central Universities (No. 202261004), the National Natural Science Foundation of China (Grant No. 91938204, 41527901, and 61701462), the Marine S and T fund of Shandong Province for Pilot National Laboratory for Marine Science and Technology (Qingdao) (No.2018SDKJ0210).

Institutional Review Board Statement: Not applicable.

Informed Consent Statement: Not applicable.

Data Availability Statement: The data were downloaded from the following website: <http://soma.ece.mcmaster.ca/ipix/index.html> (accessed on 26 June 2024). <https://radars.ac.cn/web/data/getData?dataType=DatasetofRadarDetectingSea> (accessed on 26 June 2024). For the results and code generated during the study, please contact the first author.

Acknowledgments: The authors would like to gratefully thank the anonymous reviewers for their insightful and helpful. The authors would like to appreciate the usage of the Sea-detecting X-band radar and Data Acquisition Program and the Intelligent Pixel processing X-band (IPIX) radar datasets.

Conflicts of Interest: The authors declare no conflicts of interest.

References

- Makhoul, E.; López-Martínez, C.; Broquetas, A. Exploiting Polarimetric TerraSAR-X Data for Sea Clutter Characterization. *IEEE Trans. Geosci. Remote Sens.* **2016**, *54*, 358–372.
- Shui, P.L.; Shi, X.F.; Li, X.; Feng, T.; Xia, X.Y.; Han, Y. GRNN-based predictors of UHF-band sea clutter reflectivity at low grazing angle. *IEEE Geosci. Remote Sens. Lett.* **2021**, *19*, 1–5.
- Wan, J.; Luo, F.; Zhang, Y.; Xu, X.; Yin, Y. Research on sea clutter model of emulating aircraft motion based on shore-based multichannel radar. *Int. J. Remote Sens.* **2022**, *43*, 2227–2243.
- Qingliang, L.; Jinpeng, Z.; Yushi, Z. Review on sea clutter measurement and modeling. *Chin. J. Radio Sci.* **2023**, *38*, 559–573.
- Gregers-Hansen, V.; Mital, R. An empirical sea clutter model for low grazing angles. In Proceedings of the 2009 IEEE Radar Conference, Pasadena, CA, USA, 4–8 May 2009; pp. 1–5.
- Rosenberg, L.; Watts, S. *High Grazing Angle Sea-Clutter Literature Review*; DSTO, General Document DSTO-GD-0736; Defence Science and Technology Organisation: Edinburgh, Australia, 2013.
- Watts, S.; Ward, K.; Tough, R. Modelling the shape parameter of sea clutter. In Proceedings of the 2009 International Radar Conference “Surveillance for a Safer World” (RADAR 2009), Bordeaux, France, 12–16 October 2009; pp. 1–6.
- Guidoum, N.; Soltani, F.; Mezache, A. Modeling of high-resolution radar sea clutter using two approximations of the Weibull plus thermal noise distribution. *Arab. J. Sci. Eng.* **2022**, *47*, 14957–14967.
- Yang, Y.; Xiao, S.; Wang, X.; Zhang, W.; Li, Y. Statistical distribution of polarization ratio for radar sea clutter. *Radio Sci.* **2017**, *52*, 981–987.
- Fan, Y.; Chen, D.; Chen, S.; Su, J.; Tao, M.; Guo, Z.; Wang, L. Weak Target Detection Based on Full-Polarization Scattering Features under Sea Clutter Background. *Remote Sens.* **2024**, *16*, 2987.
- Zhao, P.; Wu, Z.; Zhang, Y.; Zhang, J.; Xu, X.; Wu, J. Characterization and Modeling of Doppler Spectra for Offshore UHF-Band Sea Clutter at Low Grazing Angles. *J. Mar. Sci. Eng.* **2023**, *11*, 1901.

12. Hao, D.; Yunlong, D.; Ningbo, L.; Guoqing, W.; Jian, G. Overview and prospects of research on sea clutter property cognition. *J. Radars* **2016**, *5*, 499–516.
13. Lamont-Smith, T. An empirical model of EM scattering from steepening wave profiles derived from numerical computations. *IEEE Trans. Geosci. Remote Sens.* **2003**, *41*, 1447–1454.
14. Lamont-Smith, T.; Waseda, T.; Rheem, C.K. Measurements of the Doppler spectra of breaking waves. *IET Radar Sonar Navig.* **2007**, *1*, 149–157.
15. Lee, P.; Barter, J.; Lake, B.; Thompson, H. Lineshape analysis of breaking-wave Doppler spectra. *IEE Proc.-Radar Sonar Navig.* **1998**, *145*, 135–139.
16. Walker, D. Experimentally motivated model for low grazing angle radar Doppler spectra of the sea surface. *IEE Proc.-Radar Sonar Navig.* **2000**, *147*, 114–120.
17. Walker, D. Doppler modelling of radar sea clutter. *IEE Proc.-Radar Sonar Navig.* **2001**, *148*, 73–80.
18. Lamont-Smith, T. Investigation of the variability of Doppler spectra with radar frequency and grazing angle. *IEE Proc.-Radar Sonar Navig.* **2004**, *151*, 291–298.
19. Rosenberg, L. Characterization of high grazing angle X-band sea-clutter Doppler spectra. *IEEE Trans. Aerosp. Electron. Syst.* **2014**, *50*, 406–417.
20. Rosenberg, L. Parametric modeling of sea clutter Doppler spectra. *IEEE Trans. Geosci. Remote Sens.* **2021**, *60*, 1–9.
21. Zhao, P.; Li, X.; Zhang, J.; Zhang, Y.; Zhu, X. Scattering mechanism analysis of sea clutter at UHF band by Doppler spectrum characteristics. In Proceedings of the 32nd URSI GASS, Montreal, QC, Canada, 19–26 August 2017.
22. Li, X.; Zhang, Y.; Zhang, J. A DNN-Based Method for Sea Clutter Doppler Parameters Prediction. In Proceedings of the 2021 5th International Conference on Computer Science and Artificial Intelligence, Beijing, China, 4–6 December 2021; pp. 302–309.
23. Hu, J.; Tung, W.W.; Gao, J. Detection of low observable targets within sea clutter by structure function based multifractal analysis. *IEEE Trans. Antennas Propag.* **2006**, *54*, 136–143.
24. Chen, X.; Guan, J.; He, Y.; Zhang, J. Detection of low observable moving target in sea clutter via fractal characteristics in fractional Fourier transform domain. *IET Radar Sonar Navig.* **2013**, *7*, 635–651.
25. Stankovic, L.; Thayaparan, T.; Dakovic, M. Signal decomposition by using the S-method with application to the analysis of HF radar signals in sea-clutter. *IEEE Trans. Signal Process.* **2006**, *54*, 4332–4342.
26. Li, G.; Zhang, H.; Gao, Y.; Ma, B. Sea Clutter Suppression Using Smoothed Pseudo-Wigner–Ville Distribution–Singular Value Decomposition during Sea Spikes. *Remote Sens.* **2023**, *15*, 5360.
27. Ningyuan, S.; Xiaolong, C.; Jian, G.; Xiaoqian, M.; Ningbo, L.; University, N.A. Detection and Classification of Maritime Target with Micro-motion Based on CNNs. *J. Radars* **2018**, *7*, 565–574.
28. Fan, Y.; Li, C.; Li, D.; Li, J.; Su, J.; Tao, M. A Novel Sea Clutter Suppression Method based on Neural Network. In Proceedings of the 2021 IEEE 4th International Conference on Electronic Information and Communication Technology (ICEICT), Xi’an, China, 18–20 August 2021; pp. 437–440.
29. Monbaliu, J.; Padilla-Hernandez, R.; Hargreaves, J.C.; Albiach, J.C.C.; Luo, W.; Sclavo, M.; Guenther, H. The spectral wave model, WAM, adapted for applications with high spatial resolution. *Coast. Eng.* **2000**, *41*, 41–62.
30. Li, G.; Zhang, H.; Lyu, T.; Zhang, H. Regional significant wave height forecast in the East China Sea based on the Self-Attention ConvLSTM with SWAN model. *Ocean Eng.* **2024**, *312*, 119064.
31. Skamarock, W.C.; Klemp, J.B.; Dudhia, J.; Gill, D.O.; Barker, D.M.; Duda, M.G.; Huang, X.Y.; Wang, W.; Powers, J.G.; et al. A description of the advanced research WRF version 3. *NCAR Tech. Note* **2008**, *475*, 10–5065.
32. Carvalho, D.; Rocha, A.; Gómez-Gesteira, M.; Santos, C.S. WRF wind simulation and wind energy production estimates forced by different reanalyses: Comparison with observed data for Portugal. *Appl. Energy* **2014**, *117*, 116–126.
33. Banks, R.F.; Tiana-Alsina, J.; Baldasano, J.M.; Rocabenbosch, F.; Papayannis, A.; Solomos, S.; Tzani, C.G. Sensitivity of boundary-layer variables to PBL schemes in the WRF model based on surface meteorological observations, lidar, and radiosondes during the HygrA-CD campaign. *Atmos. Res.* **2016**, *176*, 185–201.
34. Giannaros, T.M.; Melas, D.; Ziomas, I. Performance evaluation of the Weather Research and Forecasting (WRF) model for assessing wind resource in Greece. *Renew. Energy* **2017**, *102*, 190–198.
35. Prósper, M.A.; Otero-Casal, C.; Fernández, F.C.; Miguez-Macho, G. Wind power forecasting for a real onshore wind farm on complex terrain using WRF high resolution simulations. *Renew. Energy* **2019**, *135*, 674–686.
36. Alter, J.J.; Coleman, J.O. Radar digital signal processing. In *Radar Handbook*, 3rd ed.; Skolnik, M.I., Ed.; McGraw-Hill: New York, NY, USA, 2008; Chapter 25.
37. Skamarock, W.C.; Klemp, J.B.; Dudhia, J.; Gill, D.O.; Liu, Z.; Berner, J.; Wang, W.; Powers, J.G.; Duda, M.G.; Barker, D.M. *A Description of the Advanced Research WRF Model Version 4*; National Center for Atmospheric Research: Boulder, CO, USA, 2019; p. 145.
38. Raynal, A.M.; Doerry, A.W. *Doppler Characteristics of Sea Clutter*; Technical Report; Sandia National Laboratories (SNL): Albuquerque, NM, USA; Livermore, CA, USA, 2010.

39. Lee, P.; Barter, J.; Beach, K.; Hindman, C.; Lake, B.; Rungaldier, H.; Shelton, J.; Williams, A.; Yee, R.; Yuen, H. X band microwave backscattering from ocean waves. *J. Geophys. Res. Ocean.* **1995**, *100*, 2591–2611.
40. Ward, K.D.; Watts, S.; Tough, R.J. *Sea Clutter: Scattering, the K Distribution and Radar Performance*; IET: London, UK, 2006; Volume 20.
41. Masuko, H.; Okamoto, K.; Shimada, M.; Niwa, S. Measurement of microwave backscattering signatures of the ocean surface using X band and Ka band airborne scatterometers. *J. Geophys. Res. Ocean.* **1986**, *91*, 13065–13083.
42. Trizna, D. A model for Doppler peak spectral shift for low grazing angle sea scatter. *IEEE J. Ocean. Eng.* **1985**, *10*, 368–375.
43. Lamont-Smith, T. Azimuth dependence of Doppler spectra of sea clutter at low grazing angle. *IET Radar Sonar Navig.* **2008**, *2*, 97–103.
44. Hersbach, H.; Bell, B.; Berrisford, P.; Biavati, G.; Horányi, A.; Muñoz Sabater, J.; Nicolas, J.; Peubey, C.; Radu, R.; Rozum, I.; et al. ERA5 Hourly Data on Single Levels from 1940 to Present. Copernicus Climate Change Service (C3S) Climate Data Store (CDS). 2023. Available online: <https://cds.climate.copernicus.eu/datasets/reanalysis-era5-single-levels?tab=overview> (accessed on 24 December 2024).
45. Yang, S.; Li, D.; Chen, L.; Liu, Z.; Huang, X.Y.; Pan, X. The regularized WSM6 microphysical scheme and its validation in WRF 4D-Var. *Adv. Atmos. Sci.* **2023**, *40*, 483–500.
46. Taylor, K.E. Summarizing multiple aspects of model performance in a single diagram. *J. Geophys. Res. Atmos.* **2001**, *106*, 7183–7192.
47. Ningbo, L.; Yunlong, D.; Guoqing, W.; Hao, D.; Yong, H.; Jian, G.; Xiaolong, C.; You, H. Sea-detecting X-band radar and data acquisition program. *J. Radars* **2019**, *8*, 656–667.
48. Lv, M.; Zhou, C. Study on sea clutter suppression methods based on a realistic radar dataset. *Remote Sens.* **2019**, *11*, 2721.

Disclaimer/Publisher’s Note: The statements, opinions and data contained in all publications are solely those of the individual author(s) and contributor(s) and not of MDPI and/or the editor(s). MDPI and/or the editor(s) disclaim responsibility for any injury to people or property resulting from any ideas, methods, instructions or products referred to in the content.